Multiband **k.p** Model for Tetragonal Crystals: Application to Hybrid Halide Perovskite Nanocrystals

R. Ben Aich,[†] S. Ben Radhia,[†] K. Boujdaria,[*,†] M. Chamarro,[‡] C. Testelin[‡]
E-mail: kais.boujdaria@fsb.rnu.tn

January 10, 2020

Abstract

We investigate the theoretical band structure of organic-inorganic perovskites $APbX_3$, with tetragonal crystal structure. Using D_{4h} point group symmetry properties, we derive a general 16-band Hamiltonian describing the electronic band diagram in the vicinity of the wave-vector point corresponding to the direct band-gap. For bulk crystals, a very good agreement between our predictions and experimental physical parameters, as band-gap energies and effective carrier masses, is obtained. Extending this description to three-dimensional confined hybrid halide perovskite, we calculate the size dependence of the excitonic radiative lifetime and fine structure. We describe the exciton fine structure of cube-shaped nanocrystals by an interplay of crystal-field and electron-hole exchange interaction (short- and long-range part) enhanced by confinement. Using very recent experimental results on $FAPbBr_3$ nanocrystals, we extract the bulk short-range exchange interaction in this material and predict its value in other hybrid compounds. Finally, we also predict the bright-bright and bright-dark splittings as a function of nanocrystals size.

Hybrid organic-inorganic lead halide perovskites have recently emerged as outstanding materials for a variety of optoelectronic technologies, including; light emitting diodes,[1–5] lasers,[6,7] photodetectors[8] and photovoltaic applications.[9–14] These materials crystalize with the general stoichiometry of $APbX_3$, where A is an organic cation (MethylAmmonium, MA, or FormAmidinium, FA) and X is a halide atom (Cl, Br, I). Depending on temperature, perovskite crystals are known to adopt at least three different phases:[15–20] an orthorhombic phase (with D_{2h} as the point group) at low-temperature, followed by phase transitions to tetragonal (D_{4h}) and then cubic (O_h) structures as the temperature

*To whom correspondence should be addressed
[†]Université de Carthage, Faculté des Sciences de Bizerte, LR01ES15 Laboratoire de Physique des Matériaux: Structure et Propriétés, 7021 Bizerte, Tunisia.
[‡]Sorbonne Université, CNRS, Institut des NanoSciences de Paris, F-75005, Paris, France.

is increased. A detailed review of the perovskite's symmetry can be found in the Refs.[21,22]

In the early literature,[23,24] theoretical studies of the bulk band structure (BS) of metallic perovskites led to significant debate on whether they were actually semiconductors or semimetals. More recently, the band diagram of hybrid organic-inorganic lead halide perovskites has been theoretically addressed[25–32] by using mainly the first principles calculations and we find less **k.p** calculations.[33] Taken together, the studies above have clearly demonstrated a reverse band ordering of band-edge states in $APbX_3$, compared with more conventional III-V and II-VI semiconductors. For this reason, bulk $APbX_3$ is a direct band-gap semiconductor in which the upper valence band (VB) is built from cationic Pb s-like orbitals and the lowest split-off conduction band (CB) is built from Pb p-like orbitals. Strong spin-orbit coupling in the CB[25] splits the electron states with the total angular momentum $j = 3/2$ (upper band) and $j = 1/2$ (lower band).

In spite of the great interest in hybrid perovskites, many of the fundamental band parameters such as the carrier effective masses or the Kane energies, denoted by $E_{P_{S,\rho}}$ and $E_{P_S,z}$ in the present work, remain poorly characterized and their values are still controversial. For example, Yu[33] proposed the set of $\left(E_{P_{S,\rho}} = 12.7 \text{ eV}, E_{P_S,z} = 15.3 \text{ eV}\right)$ for $MAPbI_3$, while in Ref.[34] a simple estimation of the Kane energy based on two band **k.p** model gives a value $E_{P_S} \simeq 8.3$ eV, since the definition for the Kane energy differs by a factor of 3 from the more usual definition[1]. Moreover, direct calculations of E_{P_S} predict values in the range $5.3 - 6.3$ eV for these materials.[21,35,36] These band parameter values are thus not well established in hybrid $APbX_3$ perovskite compounds, even though they determine key properties such as photon absorption probabilities and radiative lifetimes. High quality predictions and understanding of these parameters is therefore crucial for the optimization and control of exciton emission and spin dynamics in the visible-wavelength range. Consequently, it is important to develop new computational techniques that can accurately describe the band diagram of $APbX_3$.

In this work, we focus on calculations of the electronic BS of D_{4h} tetragonal perovskites within the effective mass approximation. By fixing the organic cations at the static position of the D_{4h} crystal structure, we shall derive a general 16-band **k.p** Hamiltonian (including the spin degree of freedom) for the electronic structure of bulk $APbX_3$ near the wave-vector point corresponding to the direct band-gap in the presence of spin-orbit coupling. These **k.p** calculations allow the determination of the nonparabolic energy band dispersion near the Γ-point or Z-point, as well as the interband mixing, in good agreement with others theoretical predictions. We note here that the **k.p** Hamiltonian for more common zinc-blende semiconductors differs significantly from the tetragonal perovskites[27,33] that we analyze.

Thanks to this theoretical development, we not only obtain a versatile de-

[1] This two-band **k.p** approach, oversimplified, is improved in the supplementary information (see section 4) which details our four-band **k.p** model.

scription of the electronic properties of bulk tetragonal $APbX_3$ perovskites, but we also have the tools to understand and manipulate the electronic structure of quantum confined perovskites nanostructures. Over the last few years, multilayered two-dimensional (2D) hybrid halide perovskites[37] and 1D or 0D colloidal halide nanostructures have been successfully synthetized and show great potential for solar cells and optoelectronic laser devices.[38–40] In particular, 0D colloidal nanocrystals (NCs) of hybrid perovskites have recently been shown to give single photon emission at room temperature[41–43] and then have enlarged the domain of future applications of these materials to include quantum optics. With this motivation, we shall apply the 16-band tetragonal **k.p** Hamiltonian, deduced for bulk hybrid perovskites, to calculate the role of confinement on the exciton lifetime and the exciton fine structure of 0D NCs.

Being able to account for confinement is extremely important, as the role of confinement can indeed be dramatic. For example, it is known that the optical properties of $APbX_3$ NCs are governed not by free carriers transitions but by strongly Coulomb-bound electron-hole pairs known as excitons. These band-edge excitons are the bound states, pairing an upper VB hole $\left(j_h = 1/2; j_z^h = \pm 1/2\right)$ and an electron from the lowest split-off CB ($j_e = 1/2$; $j_z^e = \pm 1/2$), leading to four exciton states: a non-optically active state (dark state), $|0_D\rangle = \left(1/\sqrt{2}\right)\left[\left|j_z^e = +1/2, j_z^h = -1/2\right\rangle - \left|j_z^e = -1/2, j_z^h = +1/2\right\rangle\right]$, with zero total angular momentum, $j = j_e + j_h = 0$, and three optically active states (bright-states), $\{|+1\rangle, |0_B\rangle, |-1\rangle\}$, with $j = 1$ and z components of angular momentum $j_z = j_z^e + j_z^h = +1,\ 0,\ -1$. Let recall that $|+1\rangle = |+1/2, +1/2\rangle$, $|0_B\rangle = \left(1/\sqrt{2}\right)[|+1/2, -1/2\rangle + |-1/2, +1/2\rangle]$ and $|-1\rangle = |-1/2, -1/2\rangle$. Due to the electron-hole exchange interaction (e-h EI), excitonic states are split into several energy sublevels with lifting of the degeneracy between dark singlet and bright multiplet excitonic states; the so-called exciton fine structure.[44–51] Predicting and providing insight into the excitonic fine structure and therefore on the NCs emission properties might help the optimization of quantum devices in domains like nanophotonics or quantum optics. Hence, a purpose of this letter is to investigate how the exciton fine structure in $APbX_3$ perovskite NCs emerges from a rich interplay between the crystal structure and the e-h EI that is enhanced by confinement effects. We exclude others mechanisms related to factors such as inversion-symmetry breaking induced by the instabilities of organic cation position[52] and shape anisotropy.

We first investigate the electronic properties of bulk perovskite compounds, $APbX_3$, using the 16-band **k.p** model model for D_{4h} group that we have developed for perovskite semiconductors. In order to focus on the essential physical insights and numerical results that we wish to discuss, the full technical details of our model can be found in Supplementary information (SI), section 1. We define the band-edge parameters, such as, the crystal-field splitting energy, the spin-orbit energy, and the anisotropic interband momentum-matrix for the x $(= y)$ and z polarizations, where the z axis is chosen to be the c-axis of the tetragonal structure. The input parameters resulting from our numerical procedure are divided in two categories. Those that are taken as adjustable parameters and those that were taken null estimating that their impact on the CB and

VB dispersions considered in the present model is very small. Among the first ones: the energies associated to the correspondent momentum matrix elements $\left(E_{P_{S,\rho}}, E_{P_{S,z}}, E_{P_\rho}, E_{P_z}, E_{P_{X,1}}, E_{P_{X,2}}, E_{P_{X,3}}\right)$ (see SI, section 1, for definition), the band-structure parameters $(L_i,\ N_j,\ M_j\ ;\ i=1,2\ ;\ j=1,2,3)$ (see section 2 in SI for definition), and the spin-orbit coupling energies $(\Delta_{C,\rho}, \Delta_{C,z})$ (see SI, section 1, for definition). They are determined by comparing the energy BS obtained from the present model with the ones given by the density functional theory calculations.[28] Among the second ones, the rest of spin-orbit coupling energies Δ_{s_C}, Δ_{s_V}, Δ_ρ, Δ_Z. In the following, we discuss the main results of **k.p** calculations for D_{4h} symmetry.

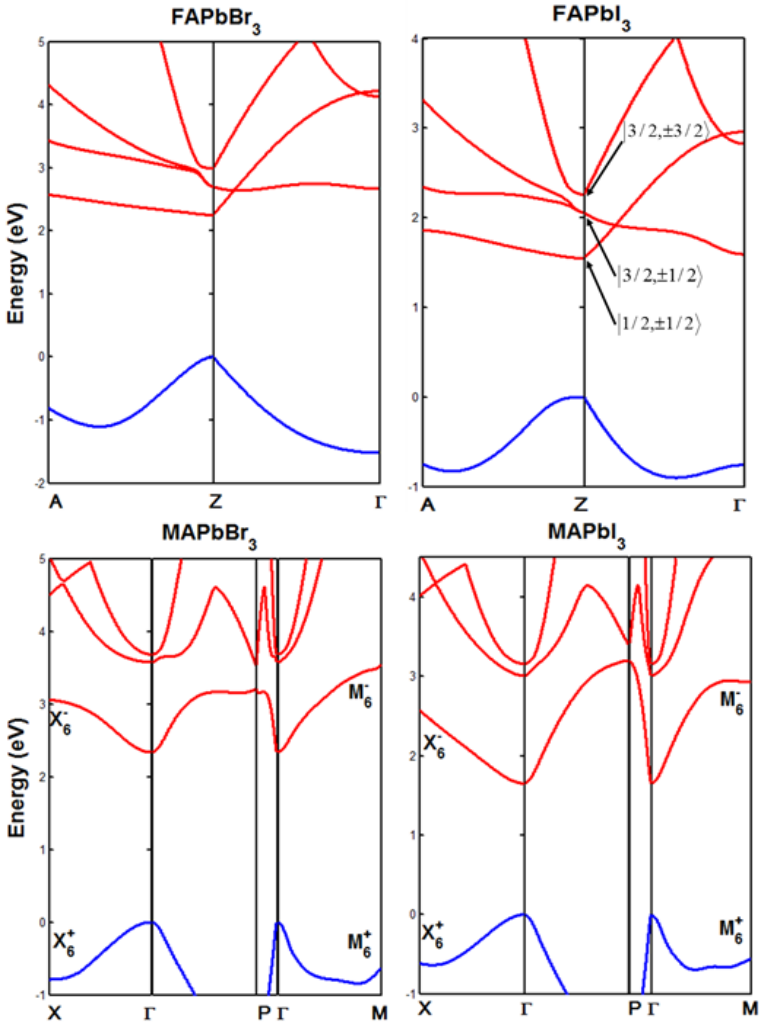

Fig .1: *The energy band structures of bulk tetragonal P4/mbm space group $FAPbX_3$ and tetragonal I4/mcm space group $MAPbX_3$ (X= Br, I) crystal*

structures obtained from the present 16-band **k.p** *model D_{4h} symmetry.*

Recent crystal structures studies of $FAPbX_3$[53,54] show that a tetragonal P4/mbm phase appears when these compounds are cooled from room temperature to lower temperatures. In contrast, $MAPbX_3$ compounds show a tetragonal crystal structure with space group I4/mcm when cooled. Figure 1 displays the band diagram of tetragonal $FAPbX_3$ and $MAPbX_3$ perovskites ($X = Br$ and I) simulated with the present 16-band **k.p** model. As shown in Fig. 1, the four materials possess a direct band gap character situated at the Z point of the Brillouin zone for FA compounds with P4/mbm space group, while the VB maximum and the CB minimum are found to be located at the center of the Brillouin zone for the MA compounds with I4/mcm as a space group. The present **k.p** model allows us to reproduce the BS of $FAPbX_3$ (X=Br, I) on a width of about 5 eV along AZ and ZΓ directions. Due to the lack of published DFT data for the band diagram of FA compounds with P4/mbm as a space group, we have considered the data given in Ref.[55] for $CsSnX_3$ as a reference while adjusting band parameters to reproduce the band-gap and carrier masses of the $FAPbX_3$ compounds. Compared to Huang and Lambrecht,[55] we obtain similar dispersions for the two considered directions. For $MAPbX_3$ ($X = Br, I$), our **k.p** approach gives good agreement for the BS over a width of about 5 eV: 1 eV across the VB and over a 4 eV scale along four directions of the lowest CBs (ΓX, ΓP, $P\Gamma$, ΓM). For the upper VB and the lowest split-off CB, the energy dispersion in the vicinity of the Γ-point is nearly isotropic. Numerical values given in Table 1 summarize the comparison of our results to those derived via the first-principles calculations,[28,56] **k.p** approach[33] or with the available experimental data given by Galkowski et al.[34] As we can see, the band-edge energies have similar magnitudes. We show a satisfactory agreement between the two approaches along ΓX direction for $MAPbBr_3$ and $MAPbI_3$ (see the values of X_6^- and X_6^+ in Table 1). Along ΓM directions, the split-off CB is reasonably well described in particular for $MAPbBr_3$ (see the values of M_6^+ in Table 1). However, we can still notice certain discrepancy for the upper VB along ΓM direction (see the values of M_6^- in Table 1). This must arise from missing interactions, especially with the d levels, which are not included within the present **k.p** model. In addition, the uncertainity in the band parameters across the literature could also contribute to such discrepancies. The difference between the band dispersions obtained from the **k.p** theory and first-principles calculations becomes significant for both second CB and second VB. Moreover, we underline that the first CB dispersion and the top VB obtained from the present 16-band **k.p** model agree well with DFT results proposed by Even *et al.*[25]

The band-gap energy, E_g, has been adjusted to be close to experimental values while fitting the band dispersion. The final E_g values are in good agreement with experimental values given in Ref.[34] (see Table 1). We observe a disagreement smaller than 4% in the worst case ($MAPbI_3$). The same behavior is retrieved when comparing our calculated band gaps with the ones given by first-principles calculations[28] and from **k.p** approach,[33] see Table 1. The parameters $\Delta_C = \sqrt{8\Delta_{C,\rho}^2 + \Delta_{C,z}^2}$, T and θ used in our calculations are also given

in Table 1 (we have taken $\Delta_{C,\rho} = \Delta_{C,z} = \Delta_C/3$). They have been estimated from the following equations that give the energy differences between the second and the first, $\left(E_2^\Gamma - E_1^\Gamma\right)$, and the third and the first electron-hole transitions, $\left(E_3^\Gamma - E_1^\Gamma\right)$, at the Γ point:

$$\begin{cases} \left(E_3^\Gamma - E_1^\Gamma\right) = \frac{1}{2}(T + 3\Delta_{C,z}) + \frac{1}{2}\left(E_2^\Gamma - E_1^\Gamma\right) \\ \left(E_2^\Gamma - E_1^\Gamma\right) = \sqrt{8\Delta_{C,\rho}^2 + \Delta_{C,z}^2 + T^2 - 2T\Delta_{C,z}} \end{cases} \quad (1)$$

where E_1^Γ, E_2^Γ and E_3^Γ are obtained from the top energies of the first VBs and the bottom of the three first CBs given in Fig. 1. Both Δ_C and T are related to θ by the relationship $\tan 2\theta = 2\sqrt{2}\ \Delta_C/(\ \Delta_C - 3T)$ (with $0 < \theta < \pi/2$), allowing us to estimate the latter parameter.

The sign and amplitude of the crystal field parameter, T, are a subject of debate.[51] We have evaluated them following recent calculations in the tetragonal phase on $CsPbBr_3$,[51] $CsPbI_3$[25] and $MAPbI_3$.[57] First-principles calculations, in absence of spin-orbit coupling, predict a positive crystal field parameter ($T > 0$) and that the Z state should be pushed at lower energy compared to the X and Y states[2]. Experimental studies are urgently needed to resolve this issue. Nonetheless, one can estimate a crystal field parameter for $MAPbI_3$ of the order of $T = 230 - 250$ meV (see figure 2 of reference[57]). We have then fixed $T = 240$ meV for the $MAPbI_3$ compound. Following the change in lattice parameter[15,53,58] and a decreasing tetragonal distortion, we have assumed a decreasing crystal field parameter when passing from Iodide to Bromide, or from MA to FA compounds. As said previously, more experimental and theoretical studies are needed, but we expect to reproduce qualitatively the crystal field parameter trend and amplitude. The present approach predicts the θ values to be in the range $38 - 40°$, which are slightly higher than the data available in the literature, namely $\theta = 24.27°$ for $MAPbI_3$[33] and $\theta = 28.66°$ for $CsPbBr_3$[47] obtained when the sign of the crystal field parameter, T, is considered negative. We can also compare the energy values of the critical points obtained in the extinctions coefficients in Ref.[59] with the energies E_1^Γ, E_2^Γ and E_3^Γ. We conclude that an additional transition is experimentally observed between E_1^Γ and E_2^Γ and it is associated to the optical transition from X_6^+ VB maximum and the minimum X_6^- of CB at X point.

The energies related to the momentum matrix elements are one of the key parameters needed to understand the optical properties of $APbX_3$ NCs. For this purpose, we focus on the Kane energies $E_{P_{S,\rho}} = (2m_0/\hbar^2)P_{S,\rho}^2$ and $E_{P_{S,z}} = (2m_0/\hbar^2)P_{S,z}^2$ which are associated to the interband momentum matrix elements $(P_{S,\rho}, P_{S,z})$ that connect the valence-band and conduction-band orbitals. $P_{S,z}$ and $P_{S,\rho}$ respectively denote the Kane parameters along and perpendicular to the c-axis of the tetragonal structure. The present **k.p** calculations predict that they are in the range $15 - 20$ eV which is slightly higher than the theoretical

[2] In presence of spin-orbit coupling, a positive sign for the crystal field parameter leads to a splitting of the conduction bands with the highest energy to the $J_z = \pm 3/2$ states. Note that an inverse order has been assumed in previously (see Ref. (33)), leading to $T < 0$. Our convention is more in agreement with recent first-principles calculations.

Table 1: Parameters determined from the 16-band **k.p** model and their comparison with the available data given in the literature.

Compound	$MAPbBr_3$			$FAPbBr_3$		$MAPbI_3$				$FAPbI_3$	
Reference	k.p	[28]	Exp [34]	k.p	Exp	k.p	[28 (56)]	[33]	Exp [34]	k.p	Exp [34]
X_6^- (eV)	3.06	3.33				2.58	2.45 (2.1)				
X_6^+ (eV)	−0.79	−0.75				−0.62	−0.65 (−0.64)				
M_6^- (eV)	3.54	3.13				2.93	2.13				
M_6^+ (eV)	−0.64	−0.46				−0.56	−0.30				
E_g (eV)	2.34	2.56	2.292	2.25	2.294[a]	1.66	1.67	1.6	1.608	1.55	1.521
Δ_C (eV)	1.65			1.5		1.42	(1.42)	1.4		1.29	
T (eV)	0.170			0.130		0.240	(0.2)	−0.7		0.205	
θ (°)	38.14			37.67	39.22[b]	40.06		24.27		39.76	
$E_{P_{S,\rho}}$ (eV)	17.97			20.01		16.45		12.68		19.04	
$E_{P_{S,z}}$ (eV)	16.45			19.75		15.36		15.33		18.25	
$m_{e\parallel}$ (m_0)	0.29	0.27		0.25		0.247	0.23	0.15		0.22	
$m_{h\parallel}$ (m_0)	0.31	0.31		0.4		0.276	0.33	0.21		0.26	
$\mu_{\parallel}(m_0)$	0.15	0.144		0.154		0.130	0.135	0.088		0.119	
$m_{e\perp}$ (m_0)	0.22			0.18		0.208		0.21		0.14	
$m_{h\perp}$ (m_0)	0.28			0.38		0.267		0.23		0.23	
$\mu_{\perp}(m_0)$	0.123		0.117	0.122	0.13[a]	0.117		0.110	0.104	0.087	0.095

[a] Reference [34]; [b] Reference [50].

results provided by Yu[33] and approximately half of the values obtained from DFT calculations for inorganic perovskites.[52] Note that using the experimental data given in Ref.,[34] the simple estimation of $E_{P_{S,\rho}}$ energy based on 4-band **k.p** model (see section 4 in SI for more details) gives $23 - 28$ eV; these values seem to be a higher bound to the $E_{P_{S,\rho}}$ energy. Moreover, we note that our $\left(E_{P_{S,\rho}}, E_{P_{S,z}}\right)$ values are very similar to the Kane energy parameters previously obtained, for more commonly studied II-VI and III-V compounds.[60]

Due to the tetragonal symmetry, the VB and CB effective masses are anisotropic. In the following, the subscript $\parallel(\perp)$ denotes along (perpendicular) to the c-axis. The values of the carrier effective masses, namely $\left(m_{e\parallel}, m_{e\perp}\right)$ and $\left(m_{h\parallel}, m_{h\perp}\right)$, extracted from the present **k.p** model (see SI, section 1) are summarized in Table 1. They are obtained from the relationships given in SI (section 3). Note that in the expressions of Eqs. (ES10–ES11), which describe the electron effective masses, the first three terms are identical with those given by Yu.[33] The additional terms, namely the $E_{P_{X,\ell}}$ $(\ell = 1, 2, 3)$ contributions, are due to the interactions between the p-like CBs and p-like VBs. In relation to Eq. (ES12), such coupling does not appear and our relationships concerning the hole effective masses are identical to the ones proposed by Yu.[33] The VB effective masses, given in Table 1, are, in general, slightly higher than the values calculated for the CB. We also note that both electron and hole effective masses are anisotropic, unlike the more conventional III-V and II-VI semiconductors for which only the hole show an anisotropic effective mass.[60] Our calculated

effective masses are in line with the theoretical predictions given in Ref.,[28] showing slightly higher values compared to DFT-GW results. Our value of $m_{e\perp} = 0.208\ m_0$ calculated for the CB minimum of $MAPbI_3$ agree very well with the value $m_{e\perp} = 0.21\ m_0$ derived from first-principles calculations using the experimental parameters,[33] while some discrepancies are observed for $m_{e\parallel}$: $(0.247\ m_0)$ versus $(0.15\ m_0)$. The same holds for the effective masses of the uppermost VB of $MAPbI_3$. Especially, the hole masses ($m_{h\parallel} = 0.276\ m_0$ and $m_{h\perp} = 0.267\ m_0$) agree with the calculations of Yu[33] which found $m_{h\parallel} = 0.21$ m_0 and $m_{h\perp} = 0.23\ m_0$. However, the results of the present work are closer to the theoretically determined masses of Ref.[28] than to the ones determined by Ref.[33] Using the $(m_{e\parallel}, m_{h\parallel})$ and $(m_{e\perp}, m_{h\perp})$ values, we determine the reduced exciton effective masses, namely $\mu_{\parallel}(m_0)$ and $\mu_{\perp}(m_0)$. Most notably, we obtain $\mu_{\parallel}(m_0) = 0.15/0.13$ for $MAPbBr_3/MAPbI_3$ which are only slightly different from the DFT-GW predictions:[28] 0.144/0.135. Moreover, the calculated $\mu_{\perp}(m_0)$ for $MAPbX_3$ and $FAPbX_3$ series ($X = Br, I$) nicely reproduce the behavior reported experimentally.[34] In conclusion, a good agreement between the whole theoretical and experimental basic physical parameters is obtained and, in particular, the present 16-band **k.p** model accurately reproduces the band gaps values and the carrier effective masses.

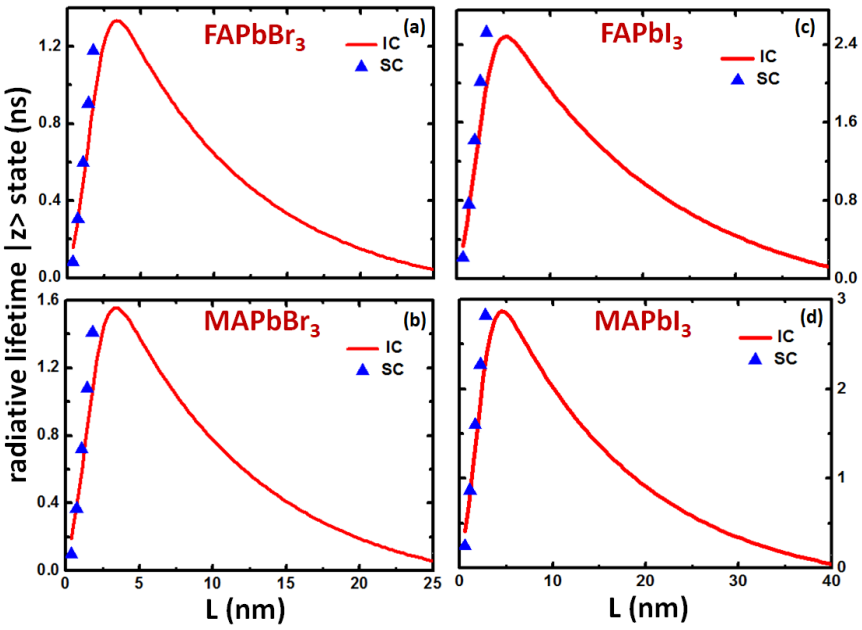

Fig. 2: *Calculated size dependence of the radiative lifetimes of the $|Z\rangle$ bright exciton for tetragonal $FAPbX_3$ and $MAPbX_3$ ($X = Br, I$) cube-shaped NCs. IC (SC) indicates the intermediate confinement (strong confinement) regime.*

The **k.p** formalism is particularly well adapted to analyze the confinement effects on the band-edge excitons of nanostructures. Recently, different hybrid

perovskite nanostructures have been synthetized: nanoplatelets,[38,61,62] quantum wires[62,63] and NCs.[64,65] Quantum dots or NCs are specially interesting because they extend the domain of application from the photovoltaic and the nanophotonics to the quantum optics. Now, combining the **k.p** band parameters deduced in the previous sections with recent experimental results for hybrid compounds,[50] we are finally in a position to calculate the exciton radiative lifetime and the exciton fine structure splittings of hybrid perovskite NCs.

The radiative recombination probability is inversely proportional to the radiative lifetime and it is directly proportional to the NCs absorption cross section. It is thus a key quantitity for characterising and engineering optoelectronic applications. The radiative rate of band-edge excitons in bulk $APbX_3$ perovskites can be obtained by using the following expression:[66]

$$\frac{1}{\tau_{NC}} = \alpha_{FS} \frac{4n\omega}{3m_0^2c^2} \left|\langle 0| \mathbf{e}.\mathbf{p} \left|\Phi_{NC}\left(\mathbf{r}_e, \mathbf{r}_h\right)\right\rangle\right|^2 \tag{2}$$

where ω is the angular frequency of the exciton optical transition, c is the light speed in vacuum, n the refractive index of surrounding media and $\alpha_{FS} = (1/137)$. The vacuum state (no electron-hole excitations) is denoted $|0\rangle$, $\mathbf{e}$ is the light polarization vector and $\mathbf{r}_e$ and $\mathbf{r}_h$ are the electron and hole position vectors. $\Phi_{NC}\left(\mathbf{r}_e, \mathbf{r}_h\right)$ is the exciton wave function (WF) in NCs and is the product of the electron and hole Bloch functions with an exciton envelope WF, $\Psi\left(\mathbf{r}_e, \mathbf{r}_h\right)$. This WF is characterized by an excitonic "Bohr radius" a_X, and further detailed information concerning the exciton WF is given in SI (section 5). We distinguish three exciton confinement regimes in a NC, namely the strong confinement regime ($L << a_X$, with L the edge length of the cube-shape NC), the intermediate confinement regime ($L \sim a_X$) and the weak-confinement regime ($L >> a_X$). Three exciton states can be considered in the tetragonal symmetry, the degenerate $|+1\rangle$ and $|-1\rangle$ states with polarizations in the plane perpendicular to the symmetry axis and the $|0_B\rangle$ state with its polarization parallel to the symmetry axis. Recently, an orthorhombic crystal structure has been identified for $FAPbX_3$ ($X = Br, I$) NCs at temperatures below $120 - 160$ K.[41,42] In orthorhombic symmetry, the exciton states are completely non-degenerate and are linearly polarized along the crystal axes. In the following, we calculate the radiative rate of a z-polarized exciton, $1/\tau_Z$, and we use the following relationship:

$$\left(\hbar^2/m_0^2\right) \left|\langle 0| \mathbf{e}.\mathbf{p} \left|\Phi_{NC}\left(\mathbf{r}, \mathbf{r}\right)\right\rangle\right|^2 = 2P_{S,z}^2 \sin^2\theta \left|\int d\mathbf{r} \Psi\left(\mathbf{r}, \mathbf{r}\right)\right|^2 \tag{3}$$

We obtain finally $1/\tau_Z$ by taking into account the local field effect throught $\mathcal{D}^2$ parameter:

$$\frac{1}{\tau_Z} = \alpha_{FS} \frac{4n\omega E_{P_{S,z}}}{3m_0c^2} \sin^2\theta \mathcal{D}^2 \left|\int d\mathbf{r} \Psi\left(\mathbf{r}, \mathbf{r}\right)\right|^2 \tag{4}$$

For a cubic NC, the interior electric field is inhomogeneous. We have calculated the NC lifetime by using an approximation for the electric local field: we

consider that its value inside of NC is homogeneous and equal to the equivalent result for a spherical geometry. As a consequence, we obtain a lower value for the lifetime than what we would obtain with the real value of the interior local field. With this approximation, $\mathcal{D} = [3\epsilon_{out}/(2\epsilon_{out} + \epsilon_X)]$. In our calculations, the surrounding medium refractive index is taken $n = 1.6$, which yields $\epsilon_{out} = n^2$ and ϵ_X is the high-frequency (at the exciton resonance) dielectric constant, whose values are extracted from the experimental data of Ref.[59]

In Fig. 2, we present τ_Z calculated for $FAPbX_3$ and $MAPbX_3$ ($X = Br$, I) NCs in the intermediate and strong confinement regimes. We have approximated the optical transition energy by $E = \hbar\omega = E_g + (1/2)\left[2/\mu_{\perp} + 1/\mu_{//}\right](\hbar\pi/L)^2$. Fig. 2 shows that in the strong confinement regime, the predicted radiative lifetime increases with increasing NC size and that this regime is obtained when $L \lesssim a_X$. For a given NC size, moving from Bromide to Iodide, one observes an increase in τ_Z, while it slightly decreases from $MAPbI_3$ to $FAPbI_3$. Recently, time-resolved experiments at single NCs[42,50] have been performed in samples containing $FAPbI_3$ ($FAPbBr_3$) NCs with sizes ranging from 10 nm to 15 nm (8-11 nm). The excited-state lifetimes were found be around 2 n s ($\sim$ 200 p s). These results are of the same order of magnitude or slightly shorter than the calculated radiative lifetimes $\sim$ 1.7 n s ($\sim$ 600 p s) indicating probably (in the latter case) the presence of non-radiative transitions.

The e-h EI is related to the Coulomb interaction and it is greatly enhanced by quantum confinement. Experimental evidences of this enhancement has been presented for colloidal NCs of the more conventional NCs.[67–71] In the framework of the effective mass approximation, Pikus and Bir[72,73] and Denisov and Makarov[74] calculated the e-h EI in relation with the exciton fine structure splittings in bulk semiconductors. Latter, the e-h EI was reconsidered in NCs by other authors[66,75–79] for a zinc-blende symmetry that is typical of common II-VI and III-V semiconductors. Two main terms can be considered in this interaction: the so-called 'non-analytical' long range (LR) contribution and the short range (SR) analytical part. The SR (LR) term is responsible for the dark–bright (bright-bright) splitting of exciton states in most of the common semiconductors.[79] Recently, LR has been calculated to be of the order of hundreds of μeV for all-inorganic perovskites[48,80] and it has been shown that the SR has a comparable value in cubic crystal structure[52] and in tetragonal crystals when calculated for $CsPbBr_3$ by DFT methods.[51] Taking into account these results, in organic-inorganic perovskite bulk materials, both contributions have to be considered to obtain accurate bright-dark and bright-bright exciton splittings in tetragonal D_{4h} or orthorhombic D_{2h} crystal structures. In the following, we describe the method used to estimate the bulk values of SR and LR contributions to the e-h EI for $FAPbBr_3$.

The SR interaction can be written as a contact interaction with the electron and hole spin Pauli operators:[81]

$$\mathcal{H}_{exch}^{SR} = \frac{1}{2} C \left(1 - \boldsymbol{\sigma}_e . \boldsymbol{\sigma}_h\right) \delta\left(\mathbf{r}_e - \mathbf{r}_h\right) \tag{5}$$

In the bright-dark excitons basis $\{|+1\rangle, |-1\rangle, |0_B\rangle; |0_D\rangle\}$, $\mathcal{H}^{SR}_{exch}$ is defined by the matrix:

$$\mathcal{H}^{SR}_{exch} = \frac{3}{2}\Delta_{SR}\pi a_X^3 \mathcal{K} \begin{bmatrix} \alpha^2+\beta^2 & -\alpha^2+\beta^2 & 0 & 0 \\ -\alpha^2+\beta^2 & \alpha^2+\beta^2 & 0 & 0 \\ 0 & 0 & 2\gamma^2 & 0 \\ 0 & 0 & 0 & 0 \end{bmatrix} \tag{6}$$

with $\Delta_{SR} = \frac{2}{3}\left(C/\pi a_X^3\right) = \frac{2}{3}D$ and $\mathcal{K} = \int_V |\Psi(\mathbf{r},\mathbf{r})|^2 d\mathbf{r}$. $\Psi(\mathbf{r}_e,\mathbf{r}_h)$ is the exciton envelope function (SI, section 5). The D_{2h} coefficients, (α,β,γ), are defined in Ref.[48] In D_{4h} symmetry, $\alpha^2 = \beta^2 = \frac{1}{2}\cos^2\theta$ and $\gamma^2 = \sin^2\theta$.

The LR e-h EI matrix can be written in the same basis as:[48]

$$\mathcal{H}^{LR}_{exch} = \begin{bmatrix} \Sigma_d & \Sigma_{od} & 0 & 0 \\ \Sigma_{od} & \Sigma_d & 0 & 0 \\ 0 & 0 & \Sigma_z & 0 \\ 0 & 0 & 0 & 0 \end{bmatrix} \tag{7}$$

with $\Sigma_d = \Lambda E_{P_{S,\rho}}\left(\alpha^2+\beta^2\right)\pi a_X^3\mathcal{K}$, $\Sigma_{od} = \Lambda E_{P_{S,\rho}}\left(-\alpha^2+\beta^2\right)\pi a_X^3\mathcal{K}$ and $\Sigma_z = 2\Lambda E_{P_{S,z}}\gamma^2\pi a_X^3\mathcal{K}$; where $\Lambda = \left(1/3E_g^2\right)\left(\hbar^2/2m_0\right)\left(e^2/\epsilon_0\epsilon_X\right)\left(1/\pi a_X^3\right)$. One writes the bright state eigenenergies: $\Sigma_1 = (\Sigma_d - \Sigma_{od})$, $\Sigma_2 = (\Sigma_d + \Sigma_{od})$, and $\Sigma_3 = \Sigma_z$. It is then possible to define the eigenvalues and eigenstates of $\left(\mathcal{H}^{SR}_{exch} + \mathcal{H}^{LR}_{exch}\right)$:

$$\begin{cases} E_X = \left(3\Delta_{SR} + 2\Lambda E_{P_{S,\rho}}\right)\beta^2\pi a_X^3\mathcal{K} \quad ; \quad |X\rangle = \frac{1}{\sqrt{2}}\left[|+1\rangle + |-1\rangle\right] \\ E_Y = \left(3\Delta_{SR} + 2\Lambda E_{P_{S,\rho}}\right)\alpha^2\pi a_X^3\mathcal{K} \quad ; \quad |Y\rangle = \frac{1}{\sqrt{2}}\left[|+1\rangle - |-1\rangle\right] \\ E_Z = \left(3\Delta_{SR} + 2\Lambda E_{P_{S,z}}\right)\gamma^2\pi a_X^3\mathcal{K} \quad ; \quad |Z\rangle = |0_B\rangle \\ E_D = 0 \quad ; \quad |0_D\rangle \end{cases} \tag{8}$$

These excitonic energies are function of the ratio $\left[E_{P_S}/E_g^2\epsilon_X\right]$ and the Bohr radius a_X.

We obtain the bright exciton splittings (see Fig. 3):

$$\begin{cases} \Delta E_1 = \left[3\Delta_{SR} + 2\Lambda E_{P_{S,\rho}}\right](\beta^2-\alpha^2)\pi a_X^3\mathcal{K} \\ \Delta E_2 = \left[3\Delta_{SR}(\gamma^2-\alpha^2) + 2\Lambda(E_{P_{S,z}}\gamma^2 - E_{P_{S,\rho}}\alpha^2)\right]\pi a_X^3\mathcal{K} \end{cases} \tag{9}$$

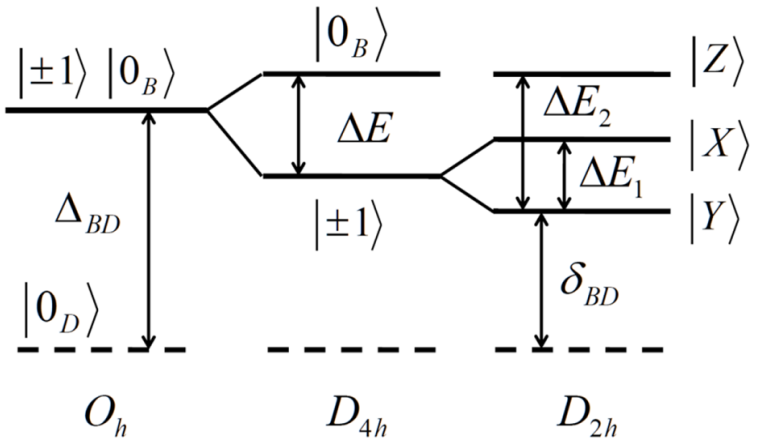

Fig. 3: *Energy labeling of the fine structure exciton states with* O_h, D_{4h} and D_{2h} symmetry.

For the D_{4h} symmetry, we obtain $\Delta E_1 = 0$ and $\Delta E_2 = \Delta E$. The bright-dark splitting is given by $\Delta_{BD} = (E_X + E_Y + E_Z)/3$ in the O_h symmetry, while we note the energy splitting between the lowest bright exciton transition and the dark exciton transition, δ_{BD}, in the D_{2h} and D_{4h} symmetries. The exciton energy labeling of the fine structure states is given in Fig. 3. Some of the numerical parameters are taken from our **k.p** calculation and experimental studies[34] (see Table 1). The others are summarized in Table 2. However very few is known about the SR parameter, Δ_{SR}, for the halide perovskites.

An intense debate has been centered on the optics of perovskite NCs, especially the "dark" or "bright" character of the lowest fine structure exciton state.[47,51,52] First studies at the level of single NC of inorganic perovskite evidenced fine structure of bright-excitons: narrow lines grouped in triplets, doublet or simple lines have been observed.[44,82–85] In addition, lifetime measurements in ensemble of NCs as a function of temperature have pointed to the existence of a long lived state,[45,46] and particular results on Mn-doped $CsPbCl_3$ NCs indicate that this dark state is the lower energy state.[49] A very recent study has obtained a spectroscopic signature of the lowest dark exciton state in $FAPbBr_3$ NCs[50] by applying a magnetic field to make it emissive. In the tetragonal phase (D_{4h}), for cube-shaped NCs with an average size $L = 9.2$ nm, Tamarat *et al*[50] measured an average bright excitonic splitting $\Delta E = 0.7$ meV and a splitting $\delta_{BD} = 2.3$ meV. From the exciton WF, in the IC regime, one obtains $\pi a_X^3 \mathcal{K} = 2.23$ for $L = 9.2$ nm (while $\pi a_X^3 \mathcal{K} = 1$ for bulk). Using equations (8-9), proportional to $\pi a_X^3 \mathcal{K}$, and the experimental values of Ref.,[50] one gets $\delta_{BD}^{Bulk} \simeq 1.0$ meV and $\Delta E^{Bulk} = 0.32$ meV. We then deduce $\Delta_{SR}^{Bulk} = 0.324$ meV and $\theta = 39.22°$. We note that this value is close to the one obtained from our 16-band **k.p** model, $\theta = 37.67°$. In the following, due to the absence of experimental data, we will use the theoretical θ values given in Table 1 to evaluate ΔE_1, ΔE_2 and δ_{BD} splittings in the other compounds. In more conventional semiconductors (GaAs, CdTe, ...), the SR contributions to the e-h EI has been

shown to be proportional to $1/a_X^3$ (see SI, section 6). Then, assuming that this a_X^{-3} law is also valid for perovskite materials and taking as a starting point the value of Δ_{SR}^{Bulk} for $FAPbBr_3$, we are able to obtain Δ_{SR}^{Bulk} values for the other hybrid compounds (see Table 2). Once Δ_{SR}^{Bulk} is defined, we determine the value of $\mathcal{K}$ in the intermediate regime as a function of the NC size and then calculate the bright-bright and the bright-dark splittings for $APbX_3$ ($X = Br, I$) (see Figure 4). For the orthorhombic phase, we have assumed the same tetragonal crystal field parameter, T, in absence of further data. We have then adjusted the orthorhombic crystal field, ϵ, to reproduce the experimental $FAPbBr_3$ exciton splitting measured by Tamarat *et al.*:[50] for $L = 9.2$ nm and $\epsilon = 70$ meV, one obtains $\Delta E_1 = 0.384$ meV and $\Delta E_2 = 0.823$ meV, the bright triplet being in very good agreement with Ref.[50] We have then kept this orthorhombic crystal field for the other compounds. We underline that, for a given NC size within the weak confinement regime, δ_{BD} is always larger for $APbBr_3$ than for $APbI_3$. This effect is inversely proportional to the a_X value. We also underline that ΔE, ΔE_1 and ΔE_2 are similar for $APbI_3$ when A is changed ($A = FA$, MA); the same behaviour is also obtained for $APbBr_3$.

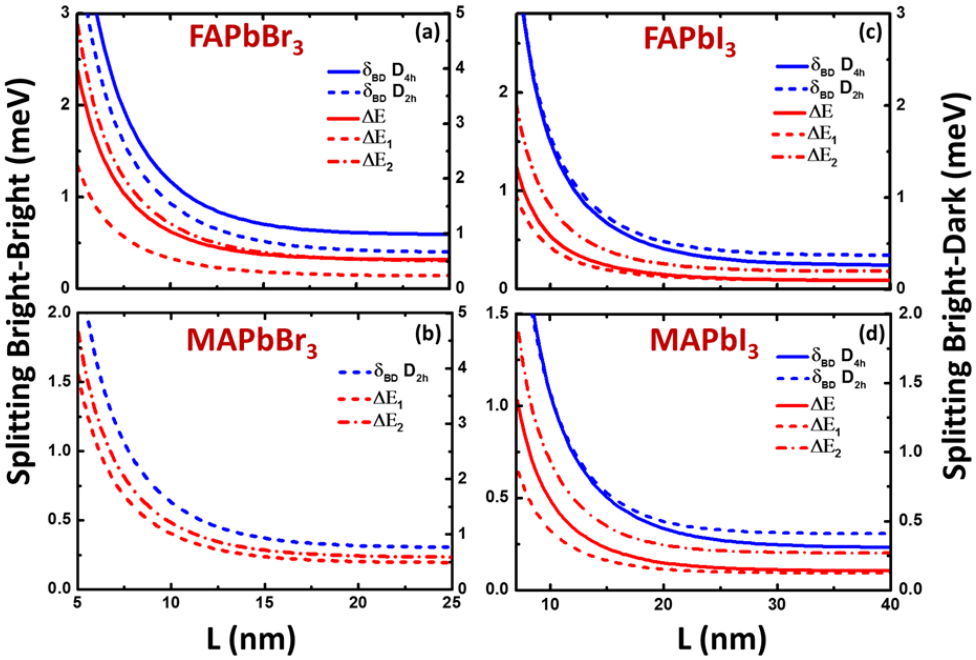

Fig. 4: *The size dependence of the exciton fine structure of tetragonal (solid lines) and orthorhombic (dot-dashed lines) $FAPbX_3$ and $MAPbX_3$ ($X = Br, I$) NCs.*

In conclusion, we have developed a description of the electronic band structure of the bulk hybrid perovskites with tetragonal crystal structure. In the

Table 2: Numerical values of the **k.p** parameters used in this work. ΔE (ΔE_1 and ΔE_2) is (are) the calculated exchange splittings for the bulk tetragonal (orthorhombic) $MAPbX_3$ and $FAPbX_3$ (X= Br, I) materials.

D_{4h}	E_g (eV)	ϵ_r	ϵ_X	a_X (nm)	$\left[E_{P_{S,\rho}}/E_g^2\epsilon_X\right]$ (eV^{-1})	Δ_{SR}^{Bulk} (meV)	ΔE (meV)	
$FAPbBr_3$[a]	2.294	8.6	5.7[b]	3.5	0.67	0.324	0.321	
$MAPbI_3$[a]	1.608	10.9	6.6[b]	5.55	0.96	0.081	0.107	
$FAPbI_3$[a]	1.521	11.4	6.4[b]	6.35	1.29	0.054	0.09	
D_{2h}	E_g (eV)	ϵ_r	ϵ_X	a_X (nm)	$\left[E_{P_{S,\rho}}/E_g^2\epsilon_X\right]$ (eV^{-1})	Δ_{SR}^{Bulk} (meV)	ΔE_1 (meV)	ΔE_2 (meV)
$MAPbBr_3$[a]	2.292	7.98	5.6[b]	3.6	0.61	0.298	0.197	0.237
$FAPbBr_3$[a]	2.233	8.42	5.7[b]	3.87	0.7	0.240	0.144	0.309
$MAPbI_3$[a]	1.652	9.4	6.6[b]	4.8	0.91	0.126	0.095	0.205
$FAPbI_3$[a]	1.501	9.35	6.4[b]	5.5	1.32	0.083	0.095	0.187

[a] Reference [34]; [b] Reference [59].

framework of the effective mass approximation, this theory reproduces the experimental values of the band gap energy and the carrier effective masses to excellent precision. Furthermore, our formalism naturally opens a route towards the understanding and prediction of the electronic properties of confined systems. We have then successfully applied this development to the study of the electronic properties of hybrid halide perovskite NCs, including crucial optoelectronic characteristics such as radiative lifetimes and the exciton fine structure. By taking into account the very few available experimental results, we are able to predict behaviours of the radiative lifetime and energy splittings of exciton fine structure states as a function of the NC size. We also predicted the value of the bulk SR contribution for all the family $APbX_3$ of perovskite compounds. The knowledge of all these electronic parameters of hybrid perovskites is of prime importance not only to improve performances of classical devices but also of quantum devices.

Acknowledgments

This work was financially supported by the Tunisian Ministry of Higher Education and Scientific research, and also by the French National Research Agency (ANR IPER-Nano2, ANR-18-CE30-0023-01).

Supporting Information Available

The Supporting Information provides background on (1) the multiband **k.p** model for D_{4h} group semiconductors, (2) the fundamental band-structure parameters (L_i, M_i, N_i), (3) the electron and hole effective masses, (4) the cubic four-band **k.p** model, (5) the band-edge exciton wave function in NCs, and (6) the dependence of the short-range parameter with the exciton Bohr radius.

References

1. Tan, Z. K.; Moghaddam, R. S.; Lai, M. L.; Docampo, P.; Higler, R.; Deschler, F.; Price, M.; Sadhanala, A.; Pazos, L. M.; Credgington, D.; et al. Bright Light-Emitting Diodes Based on Organometal Halide Perovskite. *Nat. Nanotechnol.* **2014**, *9*, 687-692.

2. Cho, H.; Jeong, S.; Park, M.; Kim, Y.; Wolf, C.; Lee, C.; Heo, H. J.; Sadhanala, A.; Myoung, N.; Yoo, S.; et al. Overcoming the Electroluminescence Efficiency Limitations of Perovskite Light-Emitting Diodes. *Science* **2015**, *350*, 1222-1225.

3. Yuan, M.; Quan, L. N.; Comin, R.; Walters, G.; Sabatini, R.; Voznyy, O.; Hoogland, S.; Zhao, Y.; Beauregard, E. M.; Kanjanaboos, P.; et al. Perovskite Energy Funnels for Efficient Light-Emitting Diodes. *Nat. Nanotechnol.* **2016,** *11*, 872-877.

4. Zhang, X.; Lin, H.; Huang, H.; Reckmeier, C.; Zhang, Y.; Choy, W. C. H.; Rogach, A. L. Enhancing the Brightness of Cesium Lead Halide Perovskite Nanocrystal Based Green Light-Emitting Devices Through the Interface Engineering with Perfluorinated Ionomer. *Nano. Lett.* **2016,** *16*, 1415-1420.

5. Kim, Y-H.; Cho, H.; Heo, J. H.; Kim,T-S.; Myoung, N.; Lee, C-L.; Im, S. H.; Lee, T-W. Multicolored Organic/Inorganic Hybrid Perovskite Light-Emitting Diodes. *Adv. Mater.* **2014**, *27***,** 1248-1254.

6. Xing, G.; Mathews, N.; Lim, S. S.; Yantara, N.; Liu, X.; Sabba, D.; Gratzel, M.; Mhaisalkar, S.; Sum, T. C. Low-Temperature Solution-Processed Wavelength-Tunable Perovskites for Lasing. *Nat. Mater.* **2014**, *13*, 476-480.

7. Zhu, H.; Fu, Y.; Meng, F.; Wu, X.; Gong, Z.; Ding, Q.; Gustafsson, M. V.; Trinh, M. T.; Jin, S.; Zhu, X. Lead Halide Perovskite Nanowire Lasers with Low Lasing Thresholds and High Quality Factors. *Nat. Mater.* **2015**, *14*, 636-642.

8. Dou, L.; Yang, Y. M.; You, J.; Hong, Z.; Chang, W.; Li, G.; Yang, Y. Solution-Processed Hybrid Perovskite Photodetectors with High Detectivity. *Nat. Commun.* **2014**, *5*, 5404.

9. Burschka, J.; Pellet, N.; Moon, S-J.; Humphry-Baker, R.; Gao, P.; Nazeeruddin, M. K.; Grätzel, M. Sequential Deposition as a Route to High-Performance Perovskite-Sensitized Solar Cells. *Nature* **2013**, *499*, 316-319.

10. Fu, F.; Feurer, T.; Jäger, T.; Avancini, E.; Bissig, B.; Yoon, S.; Buecheler, S.; Tiwari, A. N. Low-Temperature-Processed Efficient Semi-Transparent Planar Perovskite Solar Cells for Bifacial and Tandem Applications. *Nat. Commun.* **2015**, *6*, 8932.

11. Kojima, A.; Teshima, K.; Shirai, Y.; Miyasaka, T. Organometal Halide Perovskites as Visible-Light Sensitizers for Photovoltaic Cells. *J. Am. Chem. Soc.* **2009**, *131*, 6050-6051.

12. McMeekin, D. P.; Sadoughi, G.; Rehman, W.; Eperon, G. E.; Saliba, M.; Hörantner, M. T.; Haghighirad, A.; Sakai, N.; Korte, L.; Rech, B.; et al. A Mixed-Cation Lead Mixed-Halide Perovskite Absorber for Tandem Solar Cells. *Science* **2016**, *351*, 151-155.

13. Saliba, M.; Matsui, T.; Domanski, K.; Seo, J-Y.; Ummadisingu, A.; Zakeeruddin, S. M. ; Correa-Baena, J-P.; Tress, W. R.; Abate, A.; Hagfeldt, A.; et al. Incorporation of Rubidium Cations into Perovskite Solar Cells Improves Photovoltaic Performance. *Science* **2016**, *354*, 206.

14. Tan, H.; Jain, A. ; Voznyy, O.; Lan, X.; Pelayo García de Arquer, F.; Fan, J. Z.; Quintero-Bermudez, R.; Yuan, M.; Zhang, B.; Zhao, Y.; Fan, F.; et al. Efficient and Stable Solution-Processed Planar Perovskite Solar Cells via Contact Passivation. *Science* **2017**, *355*, 722-726.

15. Poglitsch, A.; Weber, W. Dynamic Disorder in Methylammoniumtrihalogenoplumbates (II) Observed by Millimeter-Wave Spectroscopy. *J. Chem. Phys.* **1987**, *87*, 6373-6378.

16. Onoda-Yamamuro, N.; Matsuo, T.; Suga, H. Calorimetric and IR Spectroscopic Studies of Phase Transitions in Methylammonium Trihalogenoplumbates (II). *J. Phys. Chem. Solids.* **1990**, *51*, 1383-1395.

17. Yamada, K.; Funabiki, S.; Horimoto, H.; Matsui, T.; Okuda, T.; Ichiba, S. Structural Phase Transitions of the Polymorphs of $CsSnI_3$ by Means of Rietveld Analysis of the X-Ray Diffraction. *Chem. Lett.* **1991**, *20*, 801-804.

18. Kong, W.; Ye, Z.; Qi, Z.; Zhang, B.; Wang, M.; Rahimi-Imam, A.; Wu, H. Characterization of an Abnormal Photoluminescence Behavior upon Crystal-Phase Transition of Perovskite $CH_3NH_3PbI_3$. *Phys. Chem. Chem. Phys.* **2015**, *17*, 16405-16411.

19. Galkowski, K.; Mitioglu, A. A.; Surrente, A.; Yang, Z.; Maude, D. K.; Kossacki, P.; Eperon, G. E.; Wang, J.T.-W; Snaith, H. J.; Plochocka, P.; et al. Spatially Resolved Studies of the Phases and Morphology of Methylammonium and Formamidinium Lead Tri-Halide Perovskites. *J. Nanoscale.* **2017**, *9*, 3222-3230.

20. Chen, C.; Hu, X.; Lu, W.; Chang, S.; Shi, L.; Li, L.; Zhong, H.; Han, J.-B. Elucidating the Phase Transitions and Temperature-Dependent Photoluminescence of MAPbBr3 Single Crystal. *Journal of Physics D: Applied Physics.* **2018**, *51*, 045105.

21. Even, J.; Pedesseau, L.; Katan, C.; Kepenekian, M.; Laurent, J.-S.; Sapori, D.; Deleporte, E. Solid-State Physics Perspective on Hybrid Perovskite Semiconductors. *J. Phys. Chem. C* **2015**, *119*, 10161-10177.

22. Even, J. Pedestrian Guide to Symmetry Properties of the Reference Cubic Structure of 3D All-Inorganic and Hybrid Perovskites. *J. Phys. Chem. Lett.* **2015**, *6*, 2238-2242.

23. Lefebvre, I.; Lippens, P. E.; Lannoo, M.; Allan, G. Band Structure of $CsSnBr_3$. *Phys. Rev. B* **1990**, *42*, 9174-9177.

24. Bose, K.; Satpathy, S.; Jepsen, O. Semiconducting $CsSnBr_3$. *Phys. Rev. B.* **1993**, *47*, 4276-4280.

25. Even, J.; Pedesseau, L.; Jancu, J-M.; Katan, C. Importance of Spin–Orbit Coupling in Hybrid Organic/Inorganic Perovskites for Photovoltaic Applications. *J. Phys. Chem. Lett.* **2013**, *4*, 2999-3005.

26. Brivio, F.; Butler, K. T.; Walsh, A.; Van Schilfgaarde, M. Relativistic Quasiparticle Self-Consistent Electronic Structure of Hybrid Halide Perovskite Photovoltaic Absorbers. *Phys. Rev. B* **2014**, *89*, 155204.

27. Even, J.; Pedesseau, L.; Jancu, J.-M.; Katan, C. DFT and $\mathbf{k} \cdot \mathbf{p}$ Modelling of the Phase Transitions of Lead and Tin Halide Perovskites for Photovoltaic Cells. *Phys. Status Solidi RRL* **2014**, *8*, 31-35.

28. Mosconi, E.; Umari, P.; De Angelis, F. Electronic and Optical Properties of $MAPbX_3$ Perovskites (X = I, Br, Cl): a Unified DFT and GW Theoretical Analysis. *Phys. Chem. Chem.Phys.* **2016**, *18*, 27158-27164.

29. Qian, J.; Xu, B.; Tian, W. A Comprehensive Theoretical Study of Halide Perovskites ABX_3 *Organic Electronics.* **2016**, *37*, 61-73.

30. Endres, J.; Egger, D. A.; Kulbak, M.; Kerner, R. A.; Zhao, L.; Silver, S. H.; Hodes, G.; Rand, B. P.; Cahen, D.; Kronik, L.; et al. Valence and Conduction Band Densities of States of Metal Halide Perovskites: A Combined Experimental-Theoretical Study. *J. Phys. Chem. Lett.* **2016**, *7*, 2722-2729.

31. Leppert, L.; Reyes-Lillo, S. E.; Neaton, J. B. Electric Field- and Strain-Induced Rashba Effect in Hybrid Halide Perovskites. *J. Phys. Chem. Lett.* **2016**, *7*, 3683-3689.

32. Tao, S. X.; Cao, X.; Bobbert, P. A. Accurate and Efficient Band Gap Predictions of Metal Halide Perovskites Using the DFT-1/2 method: GW Accuracy with DFT Expense. *Sci. Rep.* **2017**, *7*, 14386.

33. Yu, Z. G. Effective-Mass Model and Magneto-Optical Properties in Hybrid Perovskites. *Sci. Rep.* **2016**, *6*, 28576.

34. Galkowski, K.; Mitioglu, A.; Miyata, A.; Plochocka, P.; Portugall, O.; Eperon, G. E.; Wang, J.; Stergiopoulos, T.; Stranks, S. D.; Snaith, H. J.; et al. Determination of the Exciton Binding Energy and Effective Masses for Methylammonium and Formamidinium Lead Tri-Halide Perovskite Semiconductors. *Energy Environ. Sci.* **2016**, *9*, 962-970.

35. Even, J.; Pedesseau, L.; Katan, C. Analysis of Multivalley and Multibandgap Absorption and Enhancement of Free Carriers Related to Exciton Screening in Hybrid Perovskites. *J. Phys. Chem. C* **2014**, *118*, 11566-11572.

36. Fang, H.; Raissa, R.; Abdu-Aguye, M.; Adjokatse, S.; Blake, G. R.; Even, J.; Loi, M. A. Photophysics of Organic-Inorganic Hybrid Lead Iodide Perovskite Single Crystals. *Adv. Funct. Mater.* **2015**, *25*, 2378-2385.

37. Katan, C; Mercier, N; Even, J. Quantum and Dielectric Confinement Effects in Lower-Dimensional Hybrid Perovskite Semiconductors. *Chem. Rev.* **2019**, *119*, 3140-3192.

38. Ha, S. T.; Liu, X.; Zhang, Q.; Giovanni, D.; Sum, T. C.; Xiong, Q. Synthesis of Organic–Inorganic Lead Halide Perovskite Nanoplatelets: Towards High-Performance Perovskite Solar Cells and Optoelectronic Devices. *Adv. Optical Mater* **2014**, *2*, 838-844.

39. Fu, Y.; Meng, F.; Rowley, M. B.; Thompson, B. J.; Shearer, M. J.; Ma, D.; Hamers, R. J.; Wright, J. C.; Jin, S. Solution Growth of Single Crystal Methylammonium Lead Halide Perovskite Nanostructures for Optoelectronic and Photovoltaic Applications. *J. Am. Chem. Soc.* **2015,** *137*, 5810-5818.

40. Ling, Y.; Yuan, Z.; Tian, Y.; Wang, X.; Wang. JC.; Xin, Y.; Hanson, K.; Ma, B.; Gao, H. Bright Light-Emitting Diodes Based on Organometal Halide Perovskite Nanoplatelets. *Adv. Mater.* **2016**, *28*, 305-311.

41. Pfingsten, O.; Klein, J.; Protescu, L.; Bodnarchuk, M. I.; Kovalenko, M. V.; Bacher, G. Phonon Interaction and Phase Transition in Single Formamidinium Lead Bromide Quantum Dots. *Nano. Lett.* **2018**, *18*, 4440-4446.

42. Fu, M.; Tamarat, P.; Trebbia, J-P; Bodnarchuk, M. I.; Kovalenko, M. V.; Even, J.; Lounis, B. Unraveling Exciton–Phonon Coupling in Individual FAPbI3 Nanocrystals Emitting Near-Infrared Single Photons. *Nat. Commun.* **2018**, *9*, 3318.

43. Trinh, C. T.; Minh, D. N.; Ahn, K. J.; Kang, Y.; Lee K-G. Organic–Inorganic FAPbBr3 Perovskite Quantum Dots as a Quantum Light Source: Single-Photon Emission and Blinking Behaviors. *ACS Photonics* **2018**, *512*, 4937-4943.

44. Fu, M.; Tamarat, P.; Huang, H.; Even, J.; Rogach, A. L.; Lounis, B. Neutral and Charged Exciton Fine Structure in Single Lead Halide Perovskite Nanocrystals Revealed by Magneto-optical Spectroscopy. *Nano. Lett.* **2017**, *17*, 2895-2901.

45. Canneson, D.; Shornikova, E. V.; Yakovlev, D. R.; Rogge, T.; Mitioglu, A. A.; Ballottin, M. V.; Christianen, P. C. M.; Lhuillier, E.; Bayer, M.; Biadala, L. Negatively Charged and Dark Excitons in CsPbBr3 Perovskite Nanocrystals Revealed by High Magnetic Fields. *Nano. Lett.* **2017**, *17*, 6177-6183.

46. Chen, L.; Li, B.; Zhang, C.; Huang, X.; Wang, X.; Xiao, M. Composition-Dependent Energy Splitting Between Bright and Dark Excitons in Lead Halide Perovskite Nanocrystals. *Nano. Lett.* **2018**, *18*, 2074-2080.

47. Ramade, J.; Andriambariarijaona, L. M.; Steinmetz, V.; Goubet, N.; Legrand, L.; Barisien, T.; Bernardot, F.; Testelin, C.; Lhuillier, E.; Bramati, A.; et al. Fine Structure of Excitons and Electron-Hole Exchange Energy in Polymorphic CsPbBr3 Single Nanocrystals. *Nanoscale* **2018**, *10*, 6393-6401.

48. Ben Aich, R.; Saïdi, I.; Ben Radhia, S.; Boujdaria, K.; Barisien, T.; Legrand, L.; Bernardot, F.; Chamarro, M.; Testelin, C. Bright-Exciton Splittings in Inorganic Cesium Lead Halide Perovskite Nanocrystals. *Phys. Rev. Applied* **2019**, *11*, 034042.

49. Xu, K.; Vliem, J. F.; Meijerink, A. Long-Lived Dark Exciton Emission in Mn-Doped $CsPbCl_3$ Perovskite Nanocrystals. *J. Phys. Chem. C* **2019**, *123*, 979-984.

50. Tamarat, P.; Bodnarchuk, M. I.; Trebbia, J-P.; Erni, R.; Kovalenko, M. V.; Even, J.; Lounis. B. The Ground Exciton State of Formamidinium Lead Bromide Perovskite Nanocrystals is a Singlet Dark State. *Nat. Mat*, **2019**, *18*, 717-724.

51. Sercel, P. C.; Lyons, J. L.; Wickramaratne, D.; Vaxenburg, R.; Bernstein, N.; Efros, A. L. Exciton Fine Structure in Perovskite Nanocrystals. *Nano. Lett.* **2019,** *19*, 4068-4077.

52. Becker, M. A.; Vaxenburg, R.; Nedelcu, G.; Sercel, P. C.; Shabaev, A.; Mehl, M. J.; Michopoulos, J. G.; Lambrakos, S. G.; Bernstein, N.; Lyons, J. L.; et al. Bright Triplet Excitons in Caesium Lead Halide Perovskites. *Nature* **2018**, *553*, 189-193.

53. Schueller, E. C.; Laurita, G.; Fabini, D. H.; Stoumpos, C. C.; Kanatzidis, M. G.; Seshadri, R. Crystal Structure Evolution and Notable Thermal Expansion in Hybrid Perovskites Formamidinium Tin Iodide and Formamidinium Lead Bromide. *Inorg. Chem.* **2018**, *57*, 695-701.

54. Fabini, D. H.; Stoumpos, C. C.; Laurita, G.; Kaltzoglou, A.; Kontos, A. G.; Falaras, P.; Kanatzidis, M. G.; Seshadri, R. Reentrant Structural and Optical Properties and Large Positive Thermal Expansion in Perovskite Formamidinium Lead Iodide. *Angew. Chem., Int. Ed.* **2016**, *55*, 15392-15396.

55. Huang, L-Y; Lambrecht, R. L.; Electronic Band Structure, Phonons, and Exciton Binding Energies of Halide Perovskites $CsSnCl_3$, $CsSnBr_3$, and $CsSnI_3$. *Phys. Rev. B.* **2013**, *88*, 165203.

56. Jishi, R. A.; Ta, B. O.; Sharif, A. A.; Modeling of Lead Halide Perovskites for Photovoltaic Applications, *J. Phys. Chem. C* **2014**, *118*, 28344-28349.

57. Geng, W.; Zhang, L.; Zhang, N-Y.; Lau, W-M.; Liu, L-M.; First-Principles Study of Lead Iodide Perovskite Tetragonal and Orthorhombic Phases for Photovoltaic, *J. Phys. Chem. C* **2014**, *118*, 19565-19571.

58. Weber, O. J.; Ghosh, D.; Gaines, S.; Henry, P. F.; Walker, A. B.; Islam, M. S.; Weller, M. T. Phase Behavior and Polymorphism of Formamidinium Lead Iodide, *Chem. Mater.* **2018**, *30*, 3768-3778.

59. Ndione, P. F.; Li, Z.; Zhu, K. *J.* Effects of Alloying on the Optical Properties of Organic–Inorganic Lead Halide Perovskite Thin Films. *Mater. Chem. C* **2016**, *4*, 7775-7782.

60. Karazharov, S. Kh.; Lew Yan Voon, L. C. Ab Initio Studies of the Band Parameters of III-V and II-VI Zinc-Blende Semiconductors. *Semiconductors* **2005**, *39*, 161-173.

61. Hintermayr, V. A.; Richter, A. F.; Ehrat, F.; Döblinger, M.; Vanderlinden, W.; Sichert, J. A.; Tong, Y.; Polavarapu, L.; Feldmann, J.; Urban, A. S. Tuning the Optical Properties of Perovskite Nanoplatelets through Composition and Thickness by Ligand-Assisted Exfoliation. *Adv. Mater.* **2016**, *28*, 9478-9485.

62. Vybornyi, O.; Yakunin, S.; Kovalenko, M. V. Polar-Solvent-Free Colloidal Synthesis of Highly Luminescent Alkylammonium Lead Halide Perovskite Nanocrystals. *Nanoscale* **2016**, *8*, 6278-6283.

63. Teunis, M. B.; Jana, A.; Dutta, P.; Johnson, M. A; Mandal, M.; Muhoberac, B. B.; Sardar, R. Mesoscale Growth and Assembly of Bright Luminescent Organolead Halide Perovskite Quantum Wires. *Chem. Mater.* **2016**, *28*, 5043-5054.

64. Schmidt, L. C.; Pertegás, A.; González-Carrero, S.; Malinkiewicz, O.; Agouram, S.; Mínguez Espallargas, G.; Bolink, H. J.; Galian, R. E.; Pérez-Prieto, J. Nontemplate Synthesis of $CH_3NH_3PbBr_3$ Perovskite Nanoparticles. *J. Am. Chem. Soc* **2014**, *136*, 850-853.

65. Protesescu, L.; Yakunin, S.; Bodnarchuk, M. I.; Bertolotti, F.; Masciocchi, N.; Guagliardi, A.; Kovalenko, M. V. Monodisperse Formamidinium Lead Bromide Nanocrystals with Bright and Stable Green Photoluminescence. *J. Am. Chem. Soc* **2016**, *138*, 14202-14205.

66. Efros, Al. L.; Rosen, M.; Kuno, M.; Nirmal, M.; Norris, D. J.; Bawendi, M. Band-Edge Exciton in Quantum Dots of Semiconductors with a Degenerate Valence Band: Dark and Bright Exciton States. *Phys. Rev. B* **1996**, *54*, 4843-4856.

67. Calcott, P. D. J.; Nash, K. J.; Canham, L. T.; Kane, M. J.; Brumhead, D. Identification of Radiative Transitions in Highly Porous Silicon. *J. Phys. Cond. Matter* **1993**, *5*, L91-L98.

68. Nirmal, M.; Norris, D. J.; Kuno, M.; Bawendi, M. G.; Efros, Al. L.; Rosen, M. Observation of the "Dark Exciton" in CdSe Quantum Dots. *Phys. Rev. Lett.* **1995**, *75*, 3728-3731.

69. Chamarro, M.; Gourdon, C.; Lavallard, P.; Lublinskaya, O.; Ekimov, A. I. Enhancement of Electron-Hole Exchange Interaction in CdSe Nanocrystals: A Quantum Confinement Effect. *Phys. Rev. B* **1996**, *53*, 1336-1342.

70. Micic, O. I.; Cheong, H. M.; Fu, H.; Zunger, A.; Sprague, J. R.; Mascarenhas, A.; Nozik, A. J. Size-Dependent Spectroscopy of InP Quantum Dots. *J. Phys. Chem. B* **1997**, *101*, 4904-4912.

71. Banin, U.; Lee, J. C.; Guzelian, A. A.; Kadavanich, A. V.; Alivisatos, A. P. Exchange Interaction in InAs Nanocrystal Quantum Dots. *Superlattices and Microstructures* **1997**, *22*, 559-568.

72. Pikus, G. E.; Bir, G. L. Exchange Interaction in Excitons in Semiconductors. *Zh. Eksp. Teor. Fiz.* **1971**, 60, 195-208; *Sov. Phys. JETP* **1973**, *33*, 108-114.

73. Bir, G. L.; Pikus, G. E. Symmetry and Strain Induced Effects in Semiconductors; Wiley, New York; **1975**.

74. Denisov, M. M.; Makarov, V. P. Longitudinal and Transverse Excitons in Semiconductors. *Phys. Stat. Sol. (b)* **1973**, *56*, 9-59.

75. Takagahara, T. Effects of Dielectric Confinement and Electron-Hole Exchange Interaction on Excitonic States in Semiconductor Quantum Dots. *Phys. Rev. B* **1993**, *47*, 4569-4584.

76. Romestain, R.; Fishman, G. Excitonic Wave Function, Correlation energy, Exchange energy, and Oscillator Strength in a Cubic Quantum Dot. *Phys. Rev. B* **1994**, *49*, 1774-1781.

77. Franceschetti, A.; Zunger, A. Direct Pseudopotential Calculation of Exciton Coulomb and Exchange Energies in Semiconductor Quantum Dots. *Phys. Rev. Lett.* **1997**, *78*, 915-918.

78. Goupalov, S. V.; Ivchenko, E. L. Electron-Hole Long-Range Exchange Interaction in Semiconductor Quantum Dots. *J. Crystal Growth* **1998**, *184/185*, 393-397.

79. Tong, H.; Wu, M. W. Theory of Excitons in Cubic III-V Semiconductor GaAs, InAs and GaN Quantum Dots: Fine Structure and Spin Relaxation. *Phys. Rev. B* **2011**, *83*, 235323.

80. Nestoklon, M. O.; Goupalov, S. V.; Dzhioev, R. I; Ken, O. S.; Korenev, V. L.; Kusrayev, Yu. G.; Sapega, V. F.; de Weerd, C.; Gomez, L.; Gregorkiewicz, T.; et al. Optical Orientation and Alignment of Excitons in Ensembles of Inorganic Perovskite Nanocrystals. *Phys. Rev. B* **2018**, *97*, 235304.

81. Rössler, U.; Trebin, H.-R. Exchange and Polaron Corrections for Excitons in the Degenerate-Band Case. *Phys. Rev. B.* **1981**, *23*, 1961-1970.

82. Rainò, G.; Nedelcu, G.; Protesescu, L.; Bodnarchuk, M. I.; Kovalenko, M. V.; Mahrt, R. F.; Stöferle, T. Single Cesium Lead Halide Perovskite Nanocrystals at Low Temperature: Fast Single-Photon Emission, Reduced Blinking, and Exciton Fine Structure. *ACS Nano* **2016**, *10*, 2485-2490.

83. Yin, C.; Chen, L.; Song, N.; Lv, Y.; Hu, F.; Sun, C.; Yu, W. W.; Zhang, C.; Wang, X.; Zhang, Y.; et al. Bright-Exciton Fine-Structure Splittings in Single Perovskite Nanocrystals. *Phys. Rev. Lett.* **2017**, *119*, 026401.

84. Isarov, M.; Tan, L. Z.; Bodnarchuk, M. I.; Kovalenko, M. V.; Rappe, A. M.; Lifshitz, E. Rashba Effect in a Single Colloidal CsPbBr3 Perovskite Nanocrystal Detected by Magneto-Optical Measurements. *Nano Lett.* **2017,** *17*, 5020-5026.

85. Ramade, J.; Andriambariarijaona, L. M.; Steinmetz, V.; Goubet, N.; Legrand, L.; Barisien, T.; Bernardot, F.; Testelin, C.; Lhuillier, E.; Bramati, A.; et al. Exciton-Phonon Coupling in a $CsPbBr_3$ Single Nanocrystal, Appl. Phys. Lett. **2018**, *112*, 072104.

Graphical TOC Entry